1993ApJ...418..273F

THE ASTROPHYSICAL JOURNAL, 418:273–286, 1993 November 20

THERMAL MATERIAL IN DENSE CORES: A NEW NARROW-LINE PROBE AND TECHNIQUE OF TEMPERATURE DETERMINATION

G. A. FULLER[1]
Harvard-Smithsonian Center for Astrophysics and National Radio Astronomy Observatory[2]
AND
P. C. MYERS[3]
Harvard-Smithsonian Center for Astrophysics

Received 1993 February 4; accepted 1993 May 10

ABSTRACT

A survey of dense cores in nearby dark clouds indicates that the $J = 4 \rightarrow 3$ transition of HC_3N is a good tracer of very quiescent, dense gas. High spectral resolution observations at 12 positions show the line to have a median intrinsic velocity dispersion of 0.088 km s^{-1} as compared to 0.100 km s^{-1} for new high spectral resolution measurements of the NH_3 (1, 1) transition at the same positions. The narrowest HC_3N line has an observed FWMH of only 0.14 km s^{-1}, corresponding to an intrinsic velocity dispersion of only 0.058 ± 0.002 km s^{-1}. Maps of two regions show the HC_3N emission to be spatially coincident with the NH_3 emission and to be comparable, or smaller, in extent. This coincidence, together with the similar velocities of the transitions, suggests that these two transitions are tracing the same material within these cores. Adopting a two-component model for the velocity dispersion of these lines, we estimate the kinetic temperature and the nonthermal velocity dispersion in these cores. The mean kinetic temperature derived from the velocity dispersions in the cores is 9.2 ± 0.2 K, in good agreement with the value of 10.2 ± 0.6 K determined from NH_3 observations of the same objects. The kinetic temperature of 9.2 K is also similar to the mean excitation temperature of the HC_3N line, 8.4 K. This similarity suggests that the transition is close to being thermalized and indicates that the number density in these cores is close to 3×10^4 cm^{-3}. These new temperature and nonthermal velocity dispersion determinations indicate that the nonthermal velocity dispersion increases as the 0.6 ± 0.1 power of the map size, while the total velocity dispersion increases as the 0.05 ± 0.07 power of the map size. In an equilibrium model, these relations correspond to a number density profile $n \sim r^{-1.9}$, which is very close to that expected for an isothermal sphere. The magnetic field strength whose energy density equals that of the nonthermal motions is typically 10 μG over the range of core sizes 0.02–0.11 pc.

Subject headings: ISM: clouds — ISM: kinematics and dynamics — ISM: molecules — line: profiles

1. INTRODUCTION

The width of an interstellar spectral line contains information about the velocity dispersion along the line of sight and hence is a valuable probe of the motions of the interstellar gas. It has long been known that the line widths of spectral lines from much of the interstellar medium greatly exceed the Doppler width due to the thermal motions of material. However, on the smallest scales within low-mass dense cores NH_3 observations have revealed the presence of regions of quiescent gas where thermal pressure is the dominant source of support against gravitational collapse (Myers 1983). These thermal regions are interesting as they are intimately associated with star formation (Beichman et al. 1986; Myers et al. 1987) and are important in understanding the evolution of the more widespread nonthermal motions in molecular clouds. Transitions which trace these small regions of cores are useful as their narrow line widths provide excellent probes of the velocity fields within these cores and in the vicinity of the young stars associated with many cores. Observations of several cores by Sorochenko, Tolmachev, & Winnerwisser (1986) show the $J = 4 \rightarrow 3$ transition of HC_3N to have narrow line widths which suggests that it is one of the species, similar to NH_3, which trace regions of low-velocity dispersion (Myers & Benson 1983).

A remarkable feature of the dense cores observed in NH_3 is their very uniform distribution of temperatures. For the 41 cores for which Benson & Myers (1989, hereafter BM) could determine the kinetic temperature from an excitation analysis of the NH_3 (1, 1) and (2, 2) transitions, the mean temperature was 11 K and the dispersion in the temperatures is only 3 K. If this uniformity truly reflects the physical conditions within the cores, then this constrains the heating and cooling mechanisms within the core, especially the heating by embedded young stars.

The temperature is important for models of the collapse of dense cores. Such models show the mass accretion rate, $\dot{M}$, to be given by

$$\dot{M} \sim \frac{a_{\rm eff}^3}{G}, \tag{1}$$

where G is the gravitational constant and $a_{\rm eff}$ is the effective sound speed in the collapse region and $a_{\rm eff}^2 = kT_k/m_0$, where k is Boltzmann's constant, T_k is the kinetic temperature, and m_0 is the mean molecular mass, if the collapse region is thermally dominated (Shu 1977). Thus collapsing thermal cores with temperatures 5 K and 20 K will have mass accretion rates

---

[1] Postal address: National Radio Astronomy Observatory, 949 N. Cherry Avenue, Campus Building 65, Tucson, AZ 85721; e-mail: gfuller@nrao.edu.

[2] Operated by Associated Universities, Inc., under contract with the National Science Foundation.

[3] Postal address: Harvard-Smithsonian Center For Astrophysics, 60 Garden Street, Cambridge, MA 02138; e-mail: myers@cfa.harvard.edu.

TABLE 1

OBSERVED CYANOACETYLENE HYPERFINE COMPONENTS

	CWG[a]		LL[a]		
$F' \rightarrow F$	ν (MHz)	v_i (km s^{-1})	ν (MHz)	v_i (km s^{-1})	RELATIVE INTENSITY a_i
$3 \rightarrow 2$.........	36392.2304	0	36392.2380	0	0.2381
$4 \rightarrow 3$.........	36392.3238	−0.76941	36392.3316	−0.77106	0.3125
$5 \rightarrow 4$.........	36392.3574	−1.04620	36392.3654	−1.04950	0.4074

[a] Data from Cresswell et al. (1977, CWG) and Lafferty and Lovas (1977, LL). v_i is the velocity offset from the $3 \rightarrow 2$ component.

which differ by a factor of 8, and therefore accurate temperature determinations are important to constrain the mass accretion rate in these cores and hence the formation times for stars.

A long known method to determine the kinetic temperature of a gas uses a comparison of the line widths of two tracers of the same gas to separate the thermal and nonthermal motions (Baade et al. 1933). This method has been used to determine the temperatures of H II regions from recombination line observations (Gordon & Churchwell 1970; Thum 1980 [Fig. 9]). However, it has rarely been used in molecular clouds as it requires observations of at least two transitions from species with different molecular weight which trace the same gas. In addition, these transitions need to be observed with similar resolutions and high signal-to-noise ratio. From signal-to-noise considerations the lines need to have nonthermal dispersions of comparable magnitude to the thermal dispersions. This technique was used by Barrett, Meeks, & Weinreb (1964) with H I and OH absorption toward Cas A to determine the temperature of the absorbing gas. More recently, Fiebig (1990) has applied this technique to three dense cores using observations of four to seven different transitions in each core.

Recent improvements in the efficiency of the Haystack radio telescope, coupled with its large diameter and low-noise receivers have made it possible to observe many new molecular transitions which have the potential to probe the small-scale regions of dense cores. In this paper we report on new high spectral resolution observations of the $J = 4 \rightarrow 3$ transition of HC_3N in low-mass dense cores. Section 2 discusses these observations plus new high-resolution observations of the NH_3 (1, 1) transition. In § 3 the analysis of these observations is described. The results are described in § 4, and the observed velocity dispersions are used to determine both the kinetic temperature and the nonthermal velocity dispersions in the cores. Section 5 discusses the results of the temperature and nonthermal velocity determinations. Section 6 presents the main conclusions.

2. OBSERVATIONS

Observations of the HC_3N $J = 4 \rightarrow 3$ transition at 36.4 GHz were obtained using the Haystack 37 m radio telescope[4] between 1991 July and 1992 May. The hyperfine components of HC_3N observed are listed in Table 1. These are the three strongest components of the transition, the next strongest, the $F = 4 \rightarrow 4$ and $F = 3 \rightarrow 3$ components, are less than $\frac{1}{10}$ the strength of the $F = 3 \rightarrow 2$ component.

A sample of NH_3 peak positions primarily drawn from BM were initially surveyed using a velocity resolution of 0.067 km s^{-1}. The positions observed are listed in Table 2. Those positions indicated by a lower case letter in parentheses following a core name are additional positions observed within a core. At a resolution of 0.067 km s^{-1} the $F = 5 \rightarrow 4$ and $F = 4 \rightarrow 3$ hyperfine components are poorly resolved, and so for most sources the line parameters were determined from fitting a single Gaussian component to the blend of these components. Table 3 lists the rms noise in each spectrum, and for those objects where the line was detected, the integrated intensity, the peak antenna temperature, the local standard of rest velocity, and the full width at half-maximum width of the fitted Gaussian. For some sources the line width was sufficiently small that even with this velocity resolution it was possible to fit a single Gaussian to the $F = 5 \rightarrow 4$ component alone. This is the fit reported in the table for those sources indicated by asterisk after the core name.

After the initial observations it became apparent that many of the strongest lines were poorly resolved. To obtain better measurements of the line parameters all those regions with $T_A^* \gtrsim 0.5$ K were reobserved with a velocity resolution of 0.024 km s^{-1}. Only the results of these high-resolution observations are discussed in detail in this paper. New high spectral resolution NH_3 (1, 1) observations of these sources were also obtained at the Haystack Observatory during 1991 November, and one source was observed 1992 June and one in 1992 November. These NH_3 observations had a velocity resolution of 0.037 km s^{-1}. At this resolution the correlator bandwidth was 2.0 MHz, so it was only possible to observe three of the hyperfine component groups of the NH_3 transition. The components observed are listed in Table 4. Both the HC_3N and NH_3 observations were made using in-band frequency switching. This provided very flat spectral baselines while allowing maximum time on-source.

During the period over which these observations were made the Haystack antenna was being upgraded and so the efficiency varied between observing runs. Regular pointing measurements of planets and the quasars 3C 84 and 3C 273 were made during all the observations. The quasar observations gave a mean beam size at the frequency of HC_3N of 60″ and 80″ at the NH_3 frequency. The beam efficiency of the telescope determined from observations of planets was about 33% for most of the HC_3N observations except for the observations of L260, L1517, and L1400K for which the efficiency was 22% and for L1172 and L483(a) for which the efficiency was 30%. For the NH_3 observations the beam efficiency was 31% except for L483(a) for which the efficiency was 39%. Each of the foregoing beam efficiencies is subject to a measurement error of about 15%. The typical system temperatures during the observations varied between about 120 and 300 K at 36.4 GHz and between 80 and 150 K at 23.7 GHz.

---

[4] Radio Astronomy at the Haystack Observatory of the Northeast Radio Observatory Corporation is supported by the National Science Foundation.

TABLE 2

SOURCE POSITIONS

Core	R.A. (1950)	Decl. (1950)
L1450C	$3^{h}26^{m}\ 3^{s}.1$	+31° 4′47″
B5	3 44 33.4	+32 42 30
L1489(a)	4 1 45.0	+26 11 33
L1498	4 7 50.0	+25 2 13
L1495N	4 10 44.6	+28 4 58
L1495(a)	4 11 2.7	+28 1 58
L1495	4 11 6.5	+28 1 53
L1400G	4 21 12.0	+54 51 20
L1400G(a)	4 21 12.1	+54 12 20
B217	4 24 42.5	+26 11 13
L1524	4 26 26.0	+24 29 26
L1400K	4 26 51.0	+54 45 27
TMC-2A	4 28 54.0	+24 26 27
TMC-2	4 29 43.0	+24 18 54
L1536(a)	4 30 26.0	+22 37 10
L1536	4 30 26.0	+22 36 10
L1527	4 36 49.3	+25 57 16
TMC-1C	4 38 30.0	+25 55 0
TMC-1	4 38 38.9	+25 35 0
L1517	4 52 7.2	+30 33 18
L1512	5 0 54.4	+32 39 0
L1544(a)	5 1 11.1	+25 7 40
L1544	5 1 14.0	+25 7 0
L134A	15 50 58.1	−4 26 36
L183	15 51 32.7	−2 39 30
L1681B	16 24 26.1	−24 32 51
L1696A	16 25 30.0	−24 11 32
L1709B	16 28 52.1	−23 51 13
L43B	16 31 42.0	−15 41 00
L260	16 44 22.3	−9 30 2
L234A	16 45 21.0	−10 46 33
L234E	16 45 22.6	−10 51 43
L63	16 47 21.0	+18 1 00
L483(a)	18 14 46.6	−4 40 49
L483	18 14 50.6	−4 40 49
L673A	19 18 4.6	+11 14 12
L778A	19 24 26.4	+23 52 37
L778	19 24 26.4	+23 30 0
B335	19 34 33.3	+7 27 0
L1152(a)	20 35 15.2	+67 42 6
L1152(b)	20 35 19.4	+67 42 11
L1152	20 35 24.0	+67 43 23
L1152(c)	20 35 31.0	+67 43 36
L1155C	20 43 0.0	+67 41 47
L1082C	20 50 19.5	+60 7 40
L1082A	20 52 20.7	+60 3 14
L1082B	20 52 41.0	+59 58 19
L1174	20 59 46.3	+68 1 4
L1172	21 1 45.0	+67 42 13
L1172(a)	21 1 48.6	+67 42 13
NGC 7129 FIRS2	21 42 51.7	+65 49 51
L1031B	21 45 32.0	+47 19 13
L1251A	22 30 20.3	+74 57 51
L1262A	23 23 32.2	+74 1 45

3. ANALYSIS

The spectra were first corrected for the variation of the telescope gain with elevation. The atmospheric attenuation during the observations was calculated using an atmospheric model and a correction applied to the spectra. After folding the spectra to remove the effects of the frequency switch, a baseline was removed. This baseline was typically linear but occasionally quadratic.

To determine the line parameters the high-resolution HC_3N and NH_3 spectra were fitted for the total optical depth in the transition, τ, the velocity of the line, v_0, the intrinsic velocity dispersion, σ, and the amplitude, A. The spectra were fitted using the equation

$$T(v) = A[1 - e^{-\tau(v)}] + c , \tag{2}$$

where

$$\tau(v) = \tau \sum_{i=1}^{N} a_i e^{-[(v-v_0)+v_i]^2/2\sigma^2} \tag{3}$$

using a nonlinear χ^2 minimization routine (Pauls et al. 1983; Benson 1983; BM). The constant c was to account for any residual baseline offset since the line parameters were determined using a smaller region of the spectrum than was used for the initial baseline fitting. The sum in equation (3) runs over the N hyperfine components of the transition and a_i is the relative intensity of the ith hyperfine component and v_i is its velocity separation from the fiducial frequency. These parameters for the observed hyperfine components of the HC_3N and NH_3 are listed in Tables 1 and 4, respectively.

In no case was the constant c in equation (2) statistically significantly different from zero. The amplitude A can be expressed in terms of the telescope beam efficiency, η_b, the beam filling factor f and the transition excitation temperature, T_{ex}, as

$$A = \eta_b f \frac{h\nu}{k} [J(T_{ex}) - J(T_{bg})] , \tag{4}$$

where

$$J(T) = \frac{1}{e^{h\nu/kT} - 1} \tag{5}$$

and ν is the line frequency and h and k are Planck's and Boltzmann's constants, respectively. The results of the fits to the high-resolution HC_3N and NH_3 spectra are given in Tables 5 and 6.

For two cores, L1400K and L1517, the results of fitting equation (2) suggested that the HC_3N transition has very low optical depth (Table 5). For these two cores the HC_3N line parameters were determined by fitting the function

$$T(v) = A\tau(v) + c , \tag{6}$$

which is the low optical depth limit of equation (2), to the observed spectra. Therefore, for these cores it was not possible to determine A and τ separately.

The uncertainties listed in Tables 5 and 6 are the square roots of the diagonal components of the covariance matrix from the fit to the lines. These are the best estimates of the statistical uncertainty in the individual parameters. However, the comparatively large uncertainties in some parameters, notably the intensity and the optical depth of the HC_3N, do not reflect poor total signal-to-noise in the data, as is evident by comparing the antenna temperature of the $F = 5 \rightarrow 4$ component (col. [9] in Table 5) with the rms noise in the spectrum (col. [6] in Table 5). The large uncertainties in the parameters compared to the NH_3 results arise in part because there are fewer hyperfine components with a smaller intrinsic range of intensity to constrain the fit for HC_3N and in part because A and τ in equation (2) are not independently determinable when the optical depth is low.

It was not necessary to correct the fits in Tables 5 and 6 for the resolution of the spectrometer. The full width at half-maximum (FWHM) of the narrowest line observed in 0.138 km s^{-1} which is 5.7 times greater than the spectral resolution of

TABLE 3

FITS TO LOW-RESOLUTION HC_3N OBSERVATIONS

Core	rms (K)	$\int T_A^* dv$ (K km s^{-1})	T_A^* (K)	V_{LSR} (km s^{-1})	dv (km s^{-1})
L1450C	0.08	...	...	...	...
B5	0.10	...	...	...	...
L1489	0.14	...	...	...	...
L1498*	0.10	0.13(0.03)	0.52(0.18)	7.78(0.02)	0.23(0.06)
L1495N*	0.06	0.05(0.02)	0.22(0.10)	6.41(0.04)	0.22(0.08)
L1495(a)	0.10	0.14(0.03)	0.27(0.08)	6.70(0.06)	0.49(0.11)
L1495	0.07	...	...	...	...
L1400G	0.09	...	...	...	...
L1400G(a)	0.06	...	...	...	...
B217	0.08	0.04(0.01)	0.39(0.14)	6.86(0.01)	0.11(0.03)
L1524	0.09	0.10(0.02)	0.20(0.07)	6.33(0.06)	0.46(0.12)
L1400K*	0.08	0.14(0.02)	0.57(0.15)	3.27(0.02)	0.23(0.05)
TMC-2A	0.18	...	...	...	...
TMC-2	0.09	0.40(0.03)	0.65(0.07)	6.10(0.02)	0.58(0.05)
L1536(a)	0.16	0.17(0.02)	0.44(0.08)	5.54(0.02)	0.37(0.05)
L1536	0.09	0.23(0.03)	0.42(0.08)	5.38(0.03)	0.51(0.07)
L1527	0.09	0.32(0.03)	0.53(0.08)	5.86(0.03)	0.57(0.07)
TMC-1	0.12	0.90(0.04)	1.23(0.08)	5.65(0.01)	0.69(0.03)
L1517	0.14	0.28(0.03)	0.65(0.10)	5.76(0.03)	0.41(0.04)
L1512*	0.12	0.18(0.03)	0.98(0.27)	7.08(0.02)	0.17(0.04)
L1544(a)	0.11	0.33(0.02)	0.51(0.06)	7.05(0.02)	0.61(0.06)
L1544	0.12	0.37(0.04)	0.61(0.09)	7.18(0.03)	0.57(0.06)
L134A	0.07	0.08(0.02)	0.13(0.07)	2.66(0.07)	0.54(0.24)
L183*	0.09	0.20(0.02)	0.78(0.14)	2.37(0.01)	0.25(0.03)
L1681B	0.13	...	...	...	...
L1696A	0.13	0.14(0.03)	0.29(0.10)	3.28(0.05)	0.46(0.12)
L1709B	0.12	...	...	...	...
L43B	0.06	0.13(0.02)	0.25(0.05)	0.48(0.03)	0.48(0.07)
L260*	0.08	0.16(0.02)	0.84(0.19)	3.47(0.01)	0.17(0.03)
L234A*	0.07	0.09(0.02)	0.48(0.12)	2.93(0.01)	0.19(0.03)
L234E	0.07	0.10(0.02)	0.24(0.07)	3.00(0.04)	0.38(0.08)
L63	0.05	0.18(0.02)	0.31(0.05)	5.66(0.03)	0.54(0.06)
L483	0.13	0.83(0.04)	1.26(0.09)	5.23(0.01)	0.61(0.03)
L673A	0.08	...	...	...	...
L778	0.08	...	...	...	...
L778(a)	0.11	0.17(0.07)	0.25(0.19)	9.86(0.10)	0.66(0.42)
B335	0.10	...	...	...	...
L1152(a)	0.07	0.22(0.04)	0.24(0.08)	2.85(0.08)	0.86(0.23)
L1152(b)	0.08	0.17(0.02)	0.30(0.07)	2.79(0.04)	0.52(0.08)
L1152	0.06	0.10(0.02)	0.20(0.05)	2.54(0.04)	0.46(0.07)
L1152(c)	0.08	0.09(0.02)	0.14(0.05)	2.42(0.07)	0.57(0.15)
L1155C	0.08	...	...	...	...
L1082C	0.08	0.10(0.02)	0.19(0.07)	−2.61(0.06)	0.50(0.12)
L1082A	0.08	...	...	...	...
L1082B	0.06	0.09(0.02)	0.18(0.06)	−2.43(0.06)	0.49(0.12)
L1174	0.05	0.28(0.03)	0.17(0.03)	3.14(0.10)	1.62(0.23)
L1172	0.07	0.42(0.03)	0.60(0.06)	2.71(0.01)	0.66(0.05)
L1172(a)	0.07	0.22(0.02)	0.41(0.06)	2.73(0.02)	0.50(0.05)
NGC 7129 FIRS2	0.09	...	...	...	...
L1031B	0.07	...	...	...	...
L1251A	0.08	0.16(0.03)	0.34(0.09)	−4.29(0.04)	0.45(0.08)
L1262A	0.03	0.14(0.01)	0.25(0.03)	3.83(0.02)	0.53(0.05)

NOTE.—For the sources marked with an asterisk the results shown are for a fit to the $F = 5 \rightarrow 4$ hyperfine component alone. The other entries refer to fits to the blend of the $F = 5 \rightarrow 4$ and $F = 4 \rightarrow 3$ hyperfine components.

the observations. Simulations of spectra with line parameters equal to the best-fit values for L1512 indicate that the finite resolution of the autocorrelator has no effect on the measured velocity dispersion at the level of signal-to-noise in the spectra discussed here.

4. RESULTS

As mentioned above, only the strongest sources detected were observed with high spectral resolution and are discussed in this paper. Examples of these high-resolution spectra are shown in Figures 1 and 2. Most of the cores with strong HC_3N emission are not associated with young stars. Using the cross reference of *IRAS* point sources and NH_3 cores by BM, only one core with strong HC_3N emission, L1172, has an associated young star, the criterion for association being the presence of an infrared source detected by *IRAS* within one NH_3 map full width at half-maximum diameter of the NH_3 peak. The *IRAS* observations place an upper limit on the luminosity of any undetected young stars in cores without *IRAS* sources of $\sim$0.1–1 $L_\odot$, depending on the distance to the core. Observations of L483 were not reported by BM. However, Parker (1988) found a very red *IRAS* source located very close to the

1993ApJ...418..273F

TABLE 4

Observed Ammonia Hyperfine Components

$F'_1 \rightarrow F_1$	$F' \rightarrow F$	$\Delta\nu$ (kHz	v_i (km s^{-1})	Relative Intensity a_i
$0 \rightarrow 1$.........	$1/2 \rightarrow 1/2$	−1568.972	19.851	0.0370
$0 \rightarrow 1$.........	$1/2 \rightarrow 3/2$	−1526.658	19.316	0.0740
$2 \rightarrow 1$.........	$3/2 \rightarrow 1/2$	−623.335	7.887	0.0464
$2 \rightarrow 1$.........	$5/2 \rightarrow 3/2$	−590.375	7.470	0.0834
$2 \rightarrow 1$.........	$3/2 \rightarrow 3/2$	−581.021	7.351	0.0093
$1 \rightarrow 1$.........	$1/2 \rightarrow 1/2$	−36.389	0.460	0.0185
$1 \rightarrow 1$.........	$3/2 \rightarrow 1/2$	−25.453	0.322	0.0093
$2 \rightarrow 2$.........	$5/2 \rightarrow 3/2$	−24.583	0.311	0.0167
$2 \rightarrow 2$.........	$3/2 \rightarrow 3/2$	−15.196	0.192	0.1501
$1 \rightarrow 1$.........	$1/2 \rightarrow 3/2$	5.941	−0.075	0.0093
$2 \rightarrow 2$.........	$5/2 \rightarrow 5/2$	10.463	−0.132	0.2335
$1 \rightarrow 1$.........	$3/2 \rightarrow 3/2$	16.835	−0.213	0.0463
$2 \rightarrow 2$.........	$3/2 \rightarrow 5/2$	19.832	−0.251	0.0167

Note.—The frequency offsets, $\Delta\nu$, and velocity offsets, v_i, are relative to 23.694495487 GHz. Data from Kukolich 1967 and Ho 1977.

peak of an unpublished NH_3 map of this core (P. J. Benson 1989, private communication).

There are several possible explanations for the preponderence of starless cores among the strong HC_3N sources. Suzuki et al. (1992) have suggested that HC_3N abundance decreases with increasing age of a core. Therefore the HC_3N abundance would be higher in starless cores if the starless cores are at an earlier stage of evolution than cores with stars. However, the Suzuki et al. results are based on single point measurements, as is the observation made here that the strongest HC_3N emission arises from starless cores. Given the small extent of the HC_3N emission, even a slight offset from the peak of the HC_3N distribution might be enough to account for the apparent weakness of HC_3N toward many cores. It is also possible that the NH_3 and HC_3N have different spatial distributions as is the case for one of the best known cloud cores TMC-1 (Little et al. 1979; Tölle et al. 1981; Hirahara et al. 1992). The determination of whether the HC_3N observations are offset from the peak of the emission or the emission has a different distribution from the NH_3 in some cores awaits maps of more cores, especially those with weak HC_3N emission.

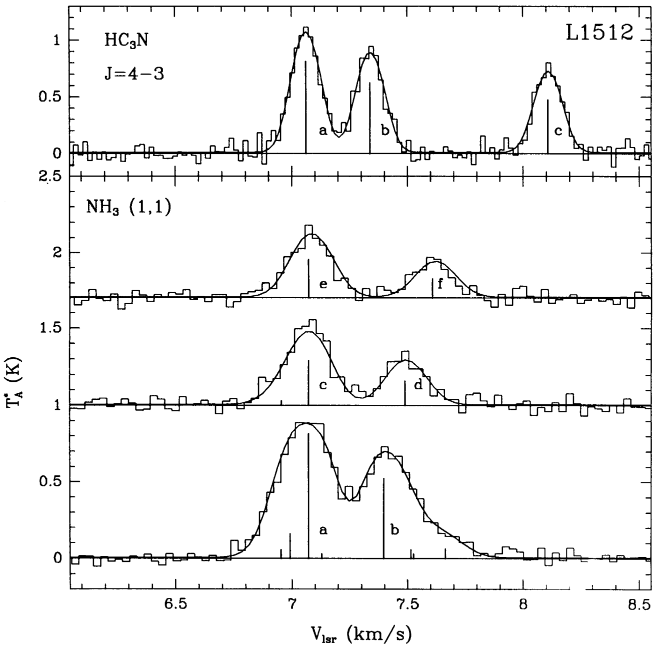

Fig. 1.—Spectra of HC_3N $J = 4 \rightarrow 3$ (*upper*) and $NH_3(1, 1)$ (*lower*) toward the core L1512. The HC_3N spectrum shows the three strongest hyperfine components of the transition. They are (*a*) $F = 5 \rightarrow 4$, (*b*) $F = 4 \rightarrow 3$, and (*c*) $F = 3 \rightarrow 2$. The strongest NH_3 hyperfine components shown are (*a*) $F'_1 \rightarrow F_1 = 2 \rightarrow 2$, $F' \rightarrow F = 5/2 \rightarrow 5/2$; (*b*) $2 \rightarrow 2$, $3/2 \rightarrow 3/2$; (*c*) $2 \rightarrow 1$, $5/2 \rightarrow 3/2$; (*d*) $2 \rightarrow 1$, $3/2 \rightarrow 1/2$; (*e*) $0 \rightarrow 1$, $1/2 \rightarrow 3/2$; and (*f*) $0 \rightarrow 1$, $1/2 \rightarrow 1/2$. The optically thin intensities of the hyperfine components used in fitting the spectra are shown schematically beneath the data. For convenience of comparison the spectra have been aligned assuming a common velocity for components *a*, *c*, and *e* of the NH_3 and component *a* of the HC_3N. For each panel the histogram shows the data and the solid curve shows the fit.

4.1. *Size of* HC_3N *Regions*

Our observations indicate that the HC_3N emission arises from very compact regions. Maps of the HC_3N emission from L483 and L1512 are presented in Figures 3 and 4. These figures also show maps of the NH_3 (1, 1) emission (BM; P. J. Benson private communication) from the same regions for comparison. The maps of L483 show the peak temperature of the $F = 5 \rightarrow 4$ component of the HC_3N and the peak temperature of the main hyperfine group of NH_3. Since the HC_3N line is so narrow in L1512 and the map was made using a spectral resolution of only 0.067 km s^{-1}, Figure 4 shows the integrated emission between 6.4 and 7.2 km s^{-1} which covers the $F = 5 \rightarrow 4$ and $F = 4 \rightarrow 3$ components of the HC_3N line. Similarly, the NH_3 map for this source shows the product of the peak temperature and velocity width of the main hyperfine component group at each position. In each contour map the heavy line indicates the half-peak contour, and the insert in the left panel shows the spatial relationship of the half-maximum contours.

Clearly in L1512 and L483 the HC_3N and NH_3 peaks are very nearly coincident and the emission from these molecules arise from very similar size regions. In L483 the HC_3N emission is almost completely contained within the region of NH_3 emission, although for L1512 the NH_3 extends somewhat

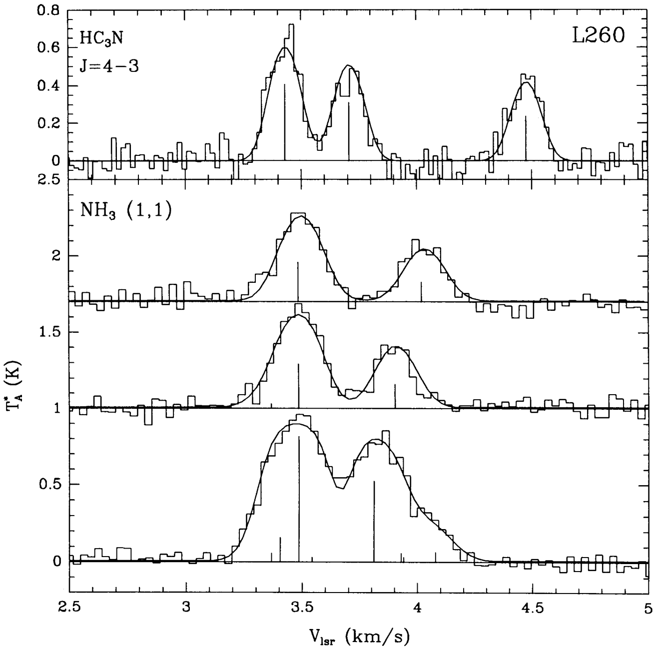

Fig. 2.—Spectra of HC_3N $J = 4 \rightarrow 3$ (*upper*) and $NH_3(1, 1)$ (*lower*) toward the core L260. The hyperfine components are the same as shown in Fig. 1.

TABLE 5

FITS TO THE HIGH RESOLUTION HC_3N SPECTRA

Core (1)	A (K) (2)	τ (nepers) (3)	V_{LSR} (km s^{-1}) (4)	σ (km s^{-1}) (5)	rms (K) (6)	χ^2 (7)	Points (8)	T_A^* (K) (9)	η_b (10)
L1498	1.47(0.16)	4.0(0.9)	7.748(0.002)	0.065(0.002)	0.08	208	221	1.19	33
L1400K	6.17(28.63)	0.2(1.1)	3.226(0.006)	0.091(0.006)	0.08	199	221	0.55	22
TMC-2	1.57(0.11)	3.0(0.4)	6.088(0.003)	0.128(0.003)	0.07	323	301	1.11	33
TMC-1C	0.90(0.07)	5.7(1.1)	5.285(0.004)	0.094(0.004)	0.08	348	301	0.81	33
L1517	2.17(4.12)	0.6(1.3)	5.737(0.005)	0.081(0.006)	0.07	190	221	0.48	22
L1512	2.34(0.77)	1.5(0.6)	7.053(0.001)	0.058(0.002)	0.06	241	221	1.08	33
L183	0.83(0.12)	4.3(1.3)	2.306(0.003)	0.076(0.004)	0.07	193	226	0.69	33
L260	0.96(0.32)	2.4(1.2)	3.422(0.003)	0.059(0.003)	0.06	221	221	0.60	22
L234A	0.61(0.22)	3.0(1.8)	2.892(0.007)	0.085(0.007)	0.08	225	221	0.44	33
L483(a)	1.15(0.05)	4.7(0.5)	5.223(0.002)	0.108(0.003)	0.06	286	301	0.98	30
L483	1.68(0.11)	3.6(0.5)	5.237(0.004)	0.130(0.004)	0.11	354	301	1.30	33
L1172	1.11(0.14)	2.0(0.4)	2.753(0.004)	0.146(0.005)	0.06	222	201	0.61	30
FITS ASSUMING THAT THE HC_3N TRANSITION IS OPTICALLY THIN									
L1400K	1.26(0.06)	...	3.227(0.006)	0.097(0.006)	0.08	141	151	0.51	22
L1517	1.18(0.05)	...	5.740(0.004)	0.079(0.004)	0.06	141	151	0.48	22

NOTE.—For the optically thin fits for L1400K and L1517 the values listed in the column headed A are the best-fit values for the product $A\tau$ since A and τ cannot be independently estimated.

The values given in cols. (2)–(5) are defined in the text (§ 3). The values in parentheses are the 1 σ uncertainties. Col. (6) is the rms noise in the spectra, col. (7) is the χ^2 of the fit, col. (8) is the number of spectral channels used in fitting the line, col. (9) is the peak antenna temperature of the $F = 5 \rightarrow 4$ hyperfine component, and col. (10) is the telescope beam efficiency.

farther to the south whereas the HC_3N possibly extends slightly farther northward. Measurements of the sizes of the half-peak contours of HC_3N and NH_3 for these two sources are given in Table 7. The size quoted is the diameter of a circle with area equal to the area of the half-maximum contour. Table 7 also lists the size after correcting for the beam size and the linear size of the emission region. The estimated uncertainty in the sizes is 0'.4. The values indicate that for both L1512 and L483 the emission from the HC_3N and NH_3 arises from regions of nearly identical sizes. This is in marked contrast to many molecular tracers in dense cores, for example, the CS $J = 2 \rightarrow 1$ and $C^{18}O$ $J = 1 \rightarrow 0$ lines. These two lines trace regions which are about twice as large as that traced by the (1, 1) line of NH_3 (Fuller 1989; Myers et al. 1991) even though the critical densities for excitation would suggest that CS should trace denser regions than are traced by the NH_3.

4.2. *Line Profiles*

The optical depths of the HC_3N and NH_3 transitions given in Tables 5 and 6 are the total optical depths, τ, as defined in equation (3). These values range from about 1 to about 6 for the HC_3N and from about 5 to 16 for the NH_3. However, the optical depths at the peak of each hyperfine component in each transition are only a fraction of these values. At the peak of strongest hyperfine component of the HC_3N, the $F = 5 \rightarrow 4$ component, the optical depth is $0.41 \times \tau(HC_3N)$. Thus, for a typical source with $\tau(HC_3N) \sim 4$ this component has a peak optical depth of only 1.6. For NH_3 where the typical source has $\tau(NH_3) \sim 10$, the strongest hyperfine component has a peak optical depth of 2.3. Therefore in these low-mass cores both of these transitions typically have peak optical depths of within a factor of 2 of unity.

TABLE 6

NH_3 FITS

Core (1)	A (K) (2)	τ (nepers) (3)	V_{LSR} (km s^{-1}) (4)	σ (km s^{-1}) (5)	rms (K) (6)	χ^2 (7)	Points (8)
L1498	1.14(0.05)	8.2(0.6)	7.799(0.002)	0.082(0.002)	0.04	389	503
L1400K	0.72(0.06)	4.8(0.6)	3.263(0.004)	0.110(0.003)	0.03	512	499
TMC-2	1.35(0.03)	9.1(0.4)	6.202(0.002)	0.105(0.002)	0.05	519	501
TMC-1C	0.80(0.03)	11.2(0.9)	5.271(0.003)	0.100(0.003)	0.05	452	500
L1517	0.72(0.02)	9.4(0.6)	5.780(0.002)	0.086(0.002)	0.03	459	503
L1512	1.02(0.04)	7.3(0.5)	7.076(0.002)	0.084(0.002)	0.04	495	503
L183	0.97(0.02)	13.1(0.5)	2.399(0.002)	0.100(0.002)	0.04	542	501
L260	0.92(0.02)	12.4(0.7)	3.490(0.002)	0.082(0.002)	0.04	509	503
L234A	1.08(0.09)	5.1(0.7)	2.936(0.004)	0.099(0.003)	0.06	516	502
L483(a)	0.93(0.01)	15.5(0.7)	5.382(0.003)	0.140(0.003)	0.06	509	500
L483	1.12(0.02)	12.0(0.5)	5.460(0.004)	0.194(0.004)	0.09	777	503
L1172	0.73(0.02)	6.8(0.4)	2.836(0.004)	0.149(0.003)	0.04	547	499

NOTE.—The values given in cols. (2)–(5) are defined in the text (§ 3). The values in parentheses are the 1 σ uncertainties. Col. (6) is the rms noise in the spectra, col. (7) is the χ^2 of the fit, col. (8) is the number of spectral channels used in fitting the line.

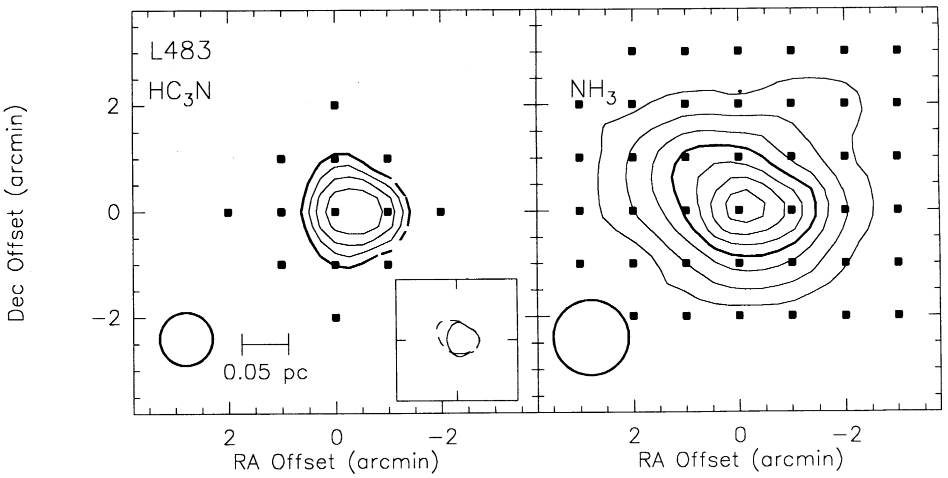

FIG. 3.—Maps of L483 showing contours of peak HC_3N emission (*left*) and peak NH_3 emission (*right*). The contour levels for the HC_3N start at 0.3 K and increase in steps of 0.1 K. The NH_3 emission shows the peak temperature of the main hyperfine group. The contour levels start at 0.1 K and increase in steps of 0.2 K. On each map the half-peak contour is indicated by the heavy contour. The insert on the HC_3N map shows the half-power contours of the HC_3N (*solid line*) and the NH_3 (*dashed lines*) superposed. The circles to the lower left of each map show the half-power beam width and the linear scale is indicated on the HC_3N map.

The χ^2 values in Table 5 and 6 indicate that, except for the NH_3 emission from L483 (discussed below), the function discussed in § 3 gives a very good fit to the data. Thus both the HC_3N and NH_3 are consistent with material within the core having a Gaussian distribution of velocities. There is no evidence for line wings or self-absorption features in these spectra.

Figure 5 shows the velocity difference between the HC_3N velocity relative to 36392.2304 MHz, the frequency of the $F = 3 \rightarrow 2$ hyperfine component quoted by Creswell, Winnewisser, and Gerry (1977) and the NH_3 velocity with respect to 23694.496 MHz (Kukolich 1967). Several things are apparent from this figure. The largest velocity discrepancy between these lines occurs in L483 where the HC_3N is blueshifted with respect to the NH_3 by more than 0.2 km s^{-1}. This corresponds to about 40% of the NH_3 line width and over 60% of the HC_3N line width. However, there is evidence that there are two velocity components present in this region (see § 5.3.2).

The remaining sources fall into three groups. For only one source, TMC-1C, is the HC_3N redshifted with respect to the NH_3 and within the uncertainties the molecules are at the same velocity. In TMC-2 and L183 the HC_3N line is blueshifted by about 0.1 km s^{-1}. The remaining seven cores form the largest group and all have the HC_3N blueshifted by about 0.04 km s^{-1} with respect to the NH_3. Although this is a small amount, it corresponds to about two resolution elements for these observations and is highly statistically significant (Fig. 5).

Velocity differences up to ± 0.034 km s^{-1} could arise from the limited accuracy of the velocity calculation used to set the local oscillator frequency at Haystack (Gordon 1976). It is possible that other instrumental effects could account for this velocity offset; however, another possible explanation is an error in the frequency of the HC_3N line. The 0.04 km s^{-1} blueshift seen for these seven cores corresponds to a 4.8 kHz frequency shift and indicates a frequency for the $F = 3 \rightarrow 2$ hyperfine component of 36392.2352 ± 0.0012 MHz where the estimated uncertainty is based on the dispersion of the velocity

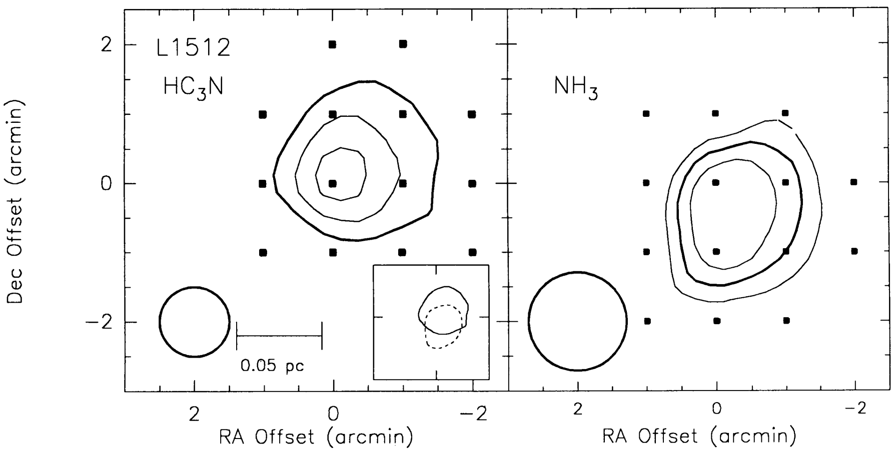

FIG. 4.—Maps of L1512 showing contours of integrated HC_3N emission (*left*) and integrated NH_3 emission (*right*). The HC_3N emission is integrated from 6.4 to 7.2 km s^{-1} which covers both the $F = 5 \rightarrow 4$ and $F = 4 \rightarrow 3$ hyperfine components. The contour levels are 0.13, 0.19, and 0.25 K km s^{-1}. The NH_3 map shows the product of the peak temperature and FWHM velocity width of the main hyperfine group. The contour levels are 0.14, 0.20, and 0.26 km s^{-1}. On each map the half-peak contour is indicated by the heavy contour. The insert on the HC_3N map shows the half-power contours of the HC_3N (*solid line*) and the NH_3 (*dashed lines*) superposed. The circles to the lower left of each map show the half-power beam width and the linear scale is indicated on the HC_3N map.

TABLE 7

FWHM MAP SIZES

		HC_3N			NH_3		
CORE	DISTANCE (pc)	Size (′)	Beam Corrected (′)	Linear Diameter (pc)	Size (′)	Beam Corrected (′)	Linear Diameter (pc)
L1512.........	140	2.1	1.8	0.075	1.9	1.4	0.055
L483	200	1.9	1.6	0.094	2.4	2.0	0.12

differences of the cores. This frequency is between the value of 36392.238 ± 0.001 MHz quoted by Lafferty & Lovas (1977) and 36392.2304 MHz from Creswell et al. (1977) (Table 1).

4.3. *Line Widths*

The HC_3N lines are remarkably narrow. The observed FWHM line widths of the $F = 3 \rightarrow 2$ hyperfine component range from 0.137 km s^{-1} for L1512 to 0.34 km s^{-1} for L1172. These are among the narrowest molecular lines known in the interstellar medium. The lines are so narrow that in several cores the $F = 5 \rightarrow 4$ and $F = 4 \rightarrow 3$ are not blended. Figures 1 and 2, which compare the HC_3N and NH_3 emission from L1512 and L260, clearly show the three main HC_3N hyperfine components. We believe that this is the first report that the $F = 5 \rightarrow 4$ and $F = 4 \rightarrow 3$ components have been individually resolved, either in the laboratory or in an astronomical observation.

Correcting for the optical depth of the transition, the intrinsic velocity dispersion of the material traced by the HC_3N emission ranges from 0.058 km s^{-1} to 0.15 km s^{-1} (Table 5). The NH_3 observations have velocity dispersions ranging from 0.082 to 0.194 km s^{-1} (Table 6). For comparison, at 10 K, the typical temperature in these cores (§ 5.1), the thermal motions of HC_3N have a dispersion of 0.040 km s^{-1} and for NH_3 the thermal dispersion is 0.070 km s^{-1}. Thus even these very narrow lines have some motions which cannot be accounted for by purely thermal motions. Figure 6 compares the velocity dispersion derived from these two tracers. In every core except TMC-2, the HC_3N dispersion is probably smaller than that of the NH_3.

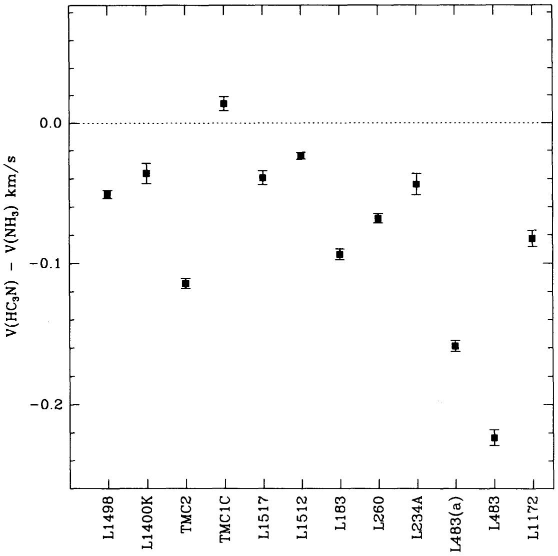

FIG. 5.—The velocity difference between the HC_3N and NH_3 emission. Values taken from Tables 5 and 6. The error bars show the 1 σ uncertainties.

The observations indicate that the HC_3N and NH_3 are tracing very similar material within the cores. The HC_3N and NH_3 transitions have similar velocities, which differ in most cases by less than a line width. Spatially, there is substantial overlap between the half-peak contours of the HC_3N and NH_3 emission mapped in two cores. In most of the cores the lines are well fitted by a single Gaussian velocity component and the dispersion of the HC_3N is less than the dispersion of the NH_3, although the line widths of both molecules indicate the presence of some nonthermal motions. Thus HC_3N is similar to NH_3 and a small group of other molecules, which includes HC_5N (Benson & Myers 1983), C_3H_2 (Cox, Walmsley, & Güsten 1989) and $C^{17}O$ (Frerking, Langer, & Wilson 1987), which trace the most quiescent regions of dense cores. Together the spatial and velocity coincidence suggests a simple model in which the NH_3 and HC_3N transition trace the same material within the cores which has some motion in excess of the purely thermal motions. The observed line dispersions can be therefore used to determine both the temperature of the core material and its nonthermal velocity dispersion using the technique first discussed by Baade et al. (1933).

4.4. *Kinetic Temperature and Nonthermal Velocity Dispersion*

The velocity dispersion of the molecular material within a core, σ, can be written as the quadrature sum of the kinetic motions and the nonthermal motions, σ_{NT}, which are defined to be the motions which are in excess of the kinetic motions,

$$\sigma^2 = \frac{kT_k}{m} + \sigma_{NT}^2 , \qquad (7)$$

where T_k is the kinetic temperature, m the molecular mass, and k is Boltzmann's constant. If two transitions trace the same material and they have the same nonthermal motions, the kinetic temperature can be written as

$$T_k = \frac{m_h m_l}{k(m_h - m_l)} (\sigma_l^2 - \sigma_h^2) , \qquad (8)$$

where the subscripts h and l refer to the heavy and light species, respectively. Equation (8) implies that the heavier molecule should have the narrower lines.

In addition to thermal dispersion, and hence the kinetic temperature, it is also possible to use the observations of these species to derive the nonthermal velocity dispersion which is given by

$$\sigma_{NT}^2 = \frac{m_h \sigma_h^2 - m_l \sigma_l^2}{m_h - m_l} . \qquad (9)$$

This two-component dispersion model can be summarized in

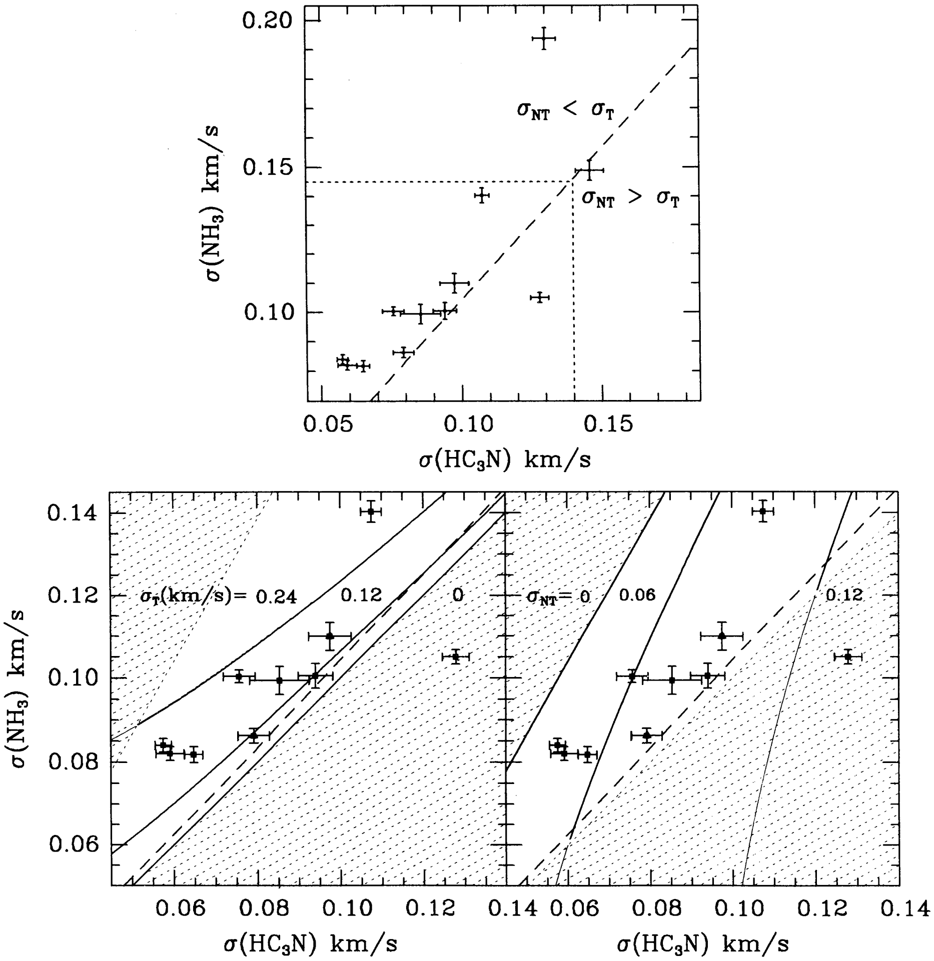

FIG. 6.—Comparison of the velocity dispersion determined from HC_3N and NH_3. The upper panel shows all the values listed in Table 8. The dashed line indicates where the thermal motions of the core material are equal to the nonthermal motions. Above this line the thermal motions dominate and below this line the nonthermal motions dominate. The region enclosed by the dotted line is expanded in the lower panels. The same data are shown on each of the lower panels. The points indicated by triangles are the optically thin fits for L1400K and L1517. The solid curves on the lower panels are curves of constant thermal velocity dispersion (*left*) and constant nonthermal velocity dispersion (*right*). The shaded regions in the lower panels indicate the areas where the model for the line widths is unphysical because $T_k < 0$ K or $\sigma_{NT} < 0$ km s^{-1}. Most of the data do not lie in these regions. The error bars show the 1 σ uncertainties.

terms of the ratio of the velocity dispersion of the light and heavy species, $s = \sigma_l/\sigma_h$. From equation (8),

$$s^2 = \frac{\sigma_{NT}^2 + \sigma_T^2 m_0/m_l}{\sigma_{NT}^2 + \sigma_T^2 m_0/m_h}, \qquad (10)$$

where

$$\sigma_T^2 = \frac{kT_k}{m_0} \qquad (11)$$

and m_0 is the mean mass of a molecule in a core which is 2.33 amu in a core comprising molecular hydrogen and 10% helium. The limiting cases are then (a) the purely nonthermal case, when $\sigma_T = 0$ and $s = s_{\min} = 1$, and (b) the purely thermal case, when $\sigma_{NT} = 0$ and $s = s_{\max} = (m_h/m_l)^{1/2}$. The critical case where $\sigma_T = \sigma_{NT}$ has $s = s_{\rm crit}$,

$$s_{\rm crit}^2 = \frac{1 + m_0/m_l}{1 + m_0/m_h}. \qquad (12)$$

For $m_l = 17$ amu and $m_h = 51$ amu, as for NH_3 and HC_3N, $s_{\rm crit} = 1.04$ and $s_{\max} = 1.73$.

Figure 6 shows the relations between the observed values of $\sigma(NH_3)$ and $\sigma(HC_3N)$ and the model values of σ_{NT} and σ_T. Figure 6*a* shows all the data from Table 8, and a dashed line indicates $\sigma(NH_3) = 1.04\ \sigma(HC_3N)$, which corresponds to $\sigma_T = \sigma_{NT}$. This figure shows that $\sigma(NH_3)$ and $\sigma(HC_3N)$ are correlated. The figure also shows that, except for TMC-2, all of these data are consistent with thermally dominated motions ($\sigma_T > \sigma_{NT}$).

Figure 6*b* shows an expanded view of the region of Figure 6*a* containing most of the data. The solid curves show lines of constant thermal velocity dispersion for the particle of mean mass, σ_T. The curve corresponding to $\sigma_T = 0$ km s^{-1} (which is the curve of $T_k = 0$ K) is also the line where $\sigma(HC_3N) = \sigma(NH_3)$ since when $T_k = 0$ K, all the observed velocity dispersion arises from the nonthermal motions common to both molecules. The shaded region to the right of this line is inaccessible within the model as it corresponds to negative temperatures. Figure 6*c* shows the same data as Figure 6*b* but the solid curves indicate lines of constant nonthermal dispersion. The shaded region to the left of the curve $\sigma_{NT} = 0$ km s^{-1} is not consistent with the model. Of the 12 positions observed in 11 cores only one core, TMC-2, definitely lies in this inaccessible

TABLE 8

TEMPERATURES

Core	T_σ (K)	$T_{ex}(HC_3N)$ (K)	$T_{ex}(NH_3)$ (K)	$T_k(NH_3)$ (K)	σ_{NT} (km s^{-1})
L1498	7.7(1.3)	9.2(0.7)	9.3(0.3)	10.1	0.054(0.004)
L1400K	7.9(3.8)	...	5.3(0.2)	10.8	0.091(0.008)
TMC-2	−16.5(2.8)	7.8(0.3)	7.5(0.1)	9.6	0.138(0.005)
TMC-1C	3.9(3.0)	5.8(0.2)	5.8(0.1)	8.0	0.091(0.007)
L1517	3.6(2.0)	...	7.1(0.1)	11.1	0.075(0.006)
L1512	11.6(1.1)	15.8(4.3)	10.7(0.3)	...	0.038(0.005)
L183	13.4(2.0)	5.6(0.4)	6.6(0.1)	9.0	0.060(0.007)
L260	10.0(1.5)	9.2(2.1)	8.1(0.1)	8.8	0.043(0.007)
L234A	8.0(4.3)	5.0(0.8)	7.5(0.4)	10.3	0.077(0.012)
L483(a)	25.1(2.8)	7.5(0.2)	6.1(0.1)	...	0.087(0.005)
L483	63.5(5.6)	9.0(0.4)	7.8(0.1)	...	0.081(0.011)
L1172	2.5(5.5)	8.1(0.7)	7.0(0.1)	14.2	0.145(0.008)

NOTE.—The kinetic temperatures determined from NH_3 observations, $T_K(NH_3)$, are from Benson & Myers 1989, except for the value for L183 which is from Ungerechts, Walmsley, & Winnewisser 1980. The results for L1400K and L1517 make use of fits to the HC_3N line which assume the emission is optically thin and hence the excitation temperature is indeterminate.

region. The remaining observations are consistent with the model of the velocity dispersion described above.

5. DISCUSSION

It is remarkable that 11 of 12 cores are consistent with a simple model for the line widths consisting of kinetic motions plus identical nonthermal motions. There are very few conveniently observable molecular lines where such a simple model is consistent with the measurements of the line widths. For example, recent DCO^+ observations show the emission arising from a similar size region to NH_3 but the DCO^+ transitions have substantially broader lines (Butner, Lada, & Loren 1993), even though DCO^+ has a molecular weight nearly twice as great as does NH_3. However, there are many mechanisms which can give rise to broadening of molecular lines such as saturation broadening and the presence of unresolved velocity gradients. In contrast, only maser amplification can decrease the observed width of a molecular transition below the local velocity dispersion and this is ruled out for most transitions, including the NH_3 and the HC_3N lines, by their low antenna temperatures and the extended nature of the emission. It is therefore the narrowest lines which least ambiguously trace the velocity dispersion within a region.

In addition to random motions it is possible that unresolved velocity gradients in the beam contribute to the observed line widths. Eight of the 11 cores have been examined for velocity gradients by Goodman et al. (1993). Of these five have velocity gradients using the Goodman et al. criteria; however, two of these are at the lower bound of the criteria. Therefore there are three sources, TMC-1C, L483 and L1172, which have significant velocity gradients. The presence of a velocity gradient has two effects for the analysis discussed here.

Assuming that the two molecules trace identical material, if the observations of the different species are made with the same angular resolution, then equation (8) shows that the velocity gradient has no effect on the derived kinetic temperatures. However, the effect of the gradient must be removed from the implied nonthermal dispersion in order to account for the contribution of the unresolved velocity gradient.

On the other hand, if the observations are made with different angular resolutions, such as the case for the observations presented here, the presence of a velocity gradient can affect both the derived temperature and the nonthermal dispersion. In this case, the effect of a velocity gradient can be estimated by subtracting the velocity shift across the appropriate beam width due to the velocity gradient from the observed line widths before calculating the temperature and nonthermal velocity dispersion. For TMC-1C, correcting for the 0.3 km s^{-1} pc^{-1} velocity measured by Goodman et al. (1993) reduces the temperature by 0.1 K. For L483 which is more distant and has a velocity gradient 7 times larger than TMC-1C, correcting for the velocity gradient decreases the temperature by 5 K and the nonthermal velocity by 0.01 km s^{-1}. For L1172 the correction reduces the temperature by 2 K and the nonthermal dispersion by 0.003 km s^{-1}. In each case these corrections are less than the uncertainty in the temperatures and nonthermal velocity dispersions. In addition, these corrections are probably upper limits as most of the material contributing to the observed line would have a velocity shift less than the extreme beam edge to beam edge shift.

5.1. *Core Temperatures*

Table 8 lists the kinetic temperature of the cores derived from the measured velocity dispersions, T_σ (Tables 5 and 6), and their uncertainties, using equation (8). The table also lists the excitation temperature of the HC_3N and NH_3 derived from the measured line intensities using equation (4). The beam filling factors used in determining the excitation temperatures of both the NH_3 and HC_3N were calculated using the sizes of the NH_3 maps made by BM. A comparison of the NH_3 excitation temperatures determined in this work with those determined by BM using lower velocity resolution spectra shows these two sets of measurements to be in excellent agreement.

The mean kinetic temperature derived from the velocity dispersion, T_σ, is 7.6 K with a standard deviation of 3.5 K. When each measurement is weighted by the inverse of its uncertainty squared the mean is 9.2 K with a standard deviation of 0.6 K and hence a standard error of the mean of 0.2 K. These values are for the sample of nine data points, which excludes TMC-2 because its line widths are inconsistent with the model, as discussed in § 5.3.1; which excludes L483 and L483(a) because their values of T_σ are unrealistic, as discussed in § 5.3.2; and which uses the optically thin fits for L1517 and L1400K, as discussed in § 3. The corresponding excitation temperatures are 8.4 K for the HC_3N and 7.5 K for the NH_3.

The kinetic temperature T_σ derived from the nine measurements discussed here has a weighted mean and standard error of the mean very similar to those derived from the (1, 1) and (2, 2) lines of NH_3 by BM. For these nine cores, the temperatures given by BM have a mean and standard error of 10.2 and 0.6 K. Here the standard error is computed with equal weighting for each meaurement, since BM do not give uncertainties on individual temperatures. The mean temperature determined from the line widths is statistically indistinguishable from the mean temperature determined from excitation analysis of the (1, 1) and (2, 2) lines of NH_3. This similarity tends to corroborate the validity of each method of temperature determination.

On the other hand, when values of T_σ are not weighted by their formal errors, their spread is considerably greater than the spread of the NH_3 kinetic temperatures. The unweighted mean and standard error of the nine T_σ measurements are 7.6 K and 1.2 K. Thus the standard error of the T_σ measurements is greater than that of the NH_3 measurements by a factor of 2. Figure 7 compares T_σ, $T_K(NH_3)$ (from Table 7 of BM),

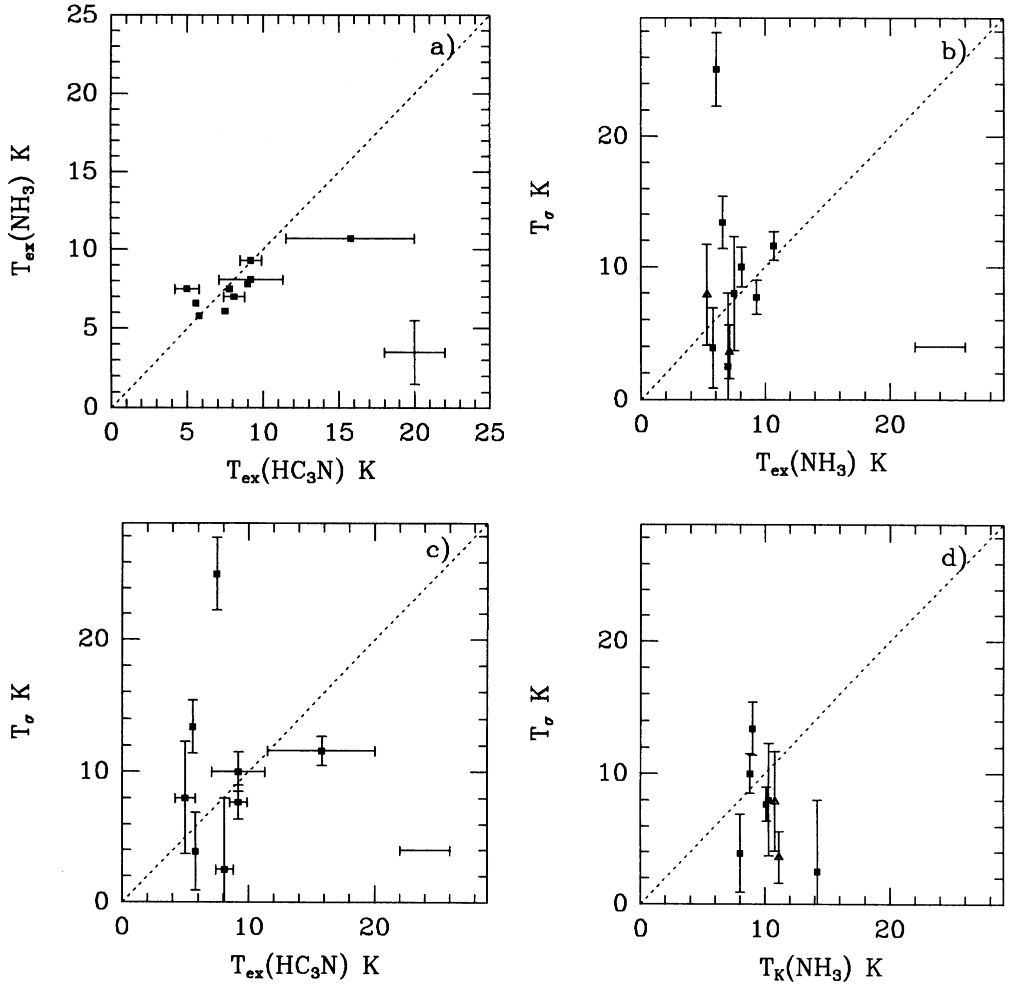

FIG. 7.—Temperature comparisons. (*a*) Comparison of the HC_3N and NH_3 excitation temperatures. Error bars (1 σ) are shown on the individual points when they significantly exceed the size of the point, and the estimated systematic uncertainties are shown at the lower right. (*b*) Comparison of the line width derived temperature T_σ and the NH_3 excitation temperature. Error bars (1 σ) are shown on the individual points when they significantly exceed the size of the point and the estimated systematic uncertainties on the excitation temperature are shown at the lower right. (*c*) Comparison of the line width derived temperature T_σ and the HC_3N excitation temperature. Error bars (1 σ) are shown on the individual points when they significantly exceed the size of the point and the estimated systematic uncertainties on the excitation temperature are shown at the lower right. (*d*) Comparison of the line width derived temperature T_σ and the NH_3 kinetic temperature from Benson & Myers (1989).

$T_{ex}(HC_3N)$, and $T_{ex}(NH_3)$ to better understand the reliability of these measures and the relations among them.

Figure 7 shows correlation plots of (*a*) excitation temperatures $T_{ex}(HC_3N)$ versus $T_{ex}(NH_3)$, (*b*) T_σ versus $T_{ex}(NH_3)$, (*c*) T_σ versus $T_{ex}(HC_3N)$, and (*d*) T_σ versus $T_k(NH_3)$. Figure 7*a* and Table 8 show that $T_{ex}(HC_3N)$ and $T_{ex}(NH_3)$ are better correlated than any of the five other pairs of temperatures. Figures 7*b* and 7*c* show that T_σ is moderately well correlated with each of $T_{ex}(HC_3N)$ and $T_{ex}(NH_3)$, particularly if the two points with $T_\sigma > 13$ K are discounted. Figure 7*d* shows that T_σ is poorly correlated with $T_k(NH_3)$, and the temperatures in Table 8 indicate that $T_k(NH_3)$ and $T_{ex}(NH_3)$ are also poorly correlated.

The good correlation of $T_{ex}(HC_3N)$ and $T_{ex}(NH_3)$ suggests that the two molecular lines sample very similar kinetic temperature and number density in each individual core. The moderate correlation of T_σ with the excitation temperature is consistent with T_σ tracing kinetic temperature, provided that most of the cores excite their lines with gas of similar density from core to core. It is therefore somewhat surprising that $T_k(NH_3)$, a well-established probe of kinetic temperature, correlates poorly with T_σ, $T_{ex}(NH_3)$, and $T_{ex}(HC_3N)$. A possible explanation of this situation is that $T_k(NH_3)$ is biased to a relatively small range of values, but has relatively large intrinsic uncertainty. These properties would account for the similarity of the mean values of $T_k(NH_3)$ and T_σ and for the poor correlation of $T_k(NH_3)$ with all other measures of temperature. In support of the possible bias of $T_k(NH_3)$ to a narrow range of temperatures, we note that when observational sensitivity limits detection of the NH_3 (2, 2) line to only the brightest sources, the resulting distribution of $T_k(NH_3)$ will be narrower than the true distribution of kinetic temperature (cf. Ho & Townes 1983, Fig. 4).

Fiebig (1990) has used a technique similar to that used in this work to determine the kinetic temperature in L1498, TMC-1C, and L1512. The temperatures derived from an analysis of seven species in L1498, 9.6 ± 1.3 K, and four species in L1512, 9.7 ± 1.3 K, are statistically indistinguishable from the 7.7 ± 1.3 K and 11.6 ± 1.1 K, respectively, measured in this work. However, from an analysis of seven species in TMC-1C

Fiebig derives a temperature of 16.0 ± 2.6 K, which is considerably larger than the 3.9 ± 3.0 K measured here and the kinetic temperature of 9.0 ± 0.3 K also determined by Fiebig from NH_3 observations. The origin of this discrepancy is unclear.

The similarity of the kinetic temperature and the HC_3N excitation temperature (Fig. 7*c*) indicates that the $J = 4 \rightarrow 3$ transition is thermalized. Therefore a lower limit on the density of the material in these cores is given by the critical density which is the density at which the spontaneous emission rate equals the collisional excitation rate. Using the collisional rates of Green & Chapman (1978) scaled for collisions with molecular hydrogen leads to a critical number density for the $J = 4 \rightarrow 3$ transition of $10^{4.6}$ $\mathrm{cm^{-3}} = 4.0 \times 10^4$ $\mathrm{cm^{-3}}$ at 10 K.

The density in these cores was also determined by BM using their NH_3 observations. For the cores observed in this work (excluding L483 which was not observed by BM) the NH_3 derived number densities range from $10^{3.8}$ $\mathrm{cm^{-3}}$ for L1400 K to $10^{5.4}$ $\mathrm{cm^{-3}}$ for L260 with a median of $10^{4.3}$ $\mathrm{cm^{-3}}$. This median value is in good agreement with the lower limit derived from the comparison of T_σ and excitation temperature.

It is interesting to note that in order to obtain reasonable fits to the observed infrared spectra of young stars in Ophiuchus, Adams, Lada, & Shu (1987) require $a_{\mathrm{eff}} = 0.35$ km $\mathrm{s^{-1}}$ which corresponds to a temperature of 35 K, considerably in excess of the 11 K necessary to fit the observations in Taurus. However, the three sources observed in this work in Ophiuchus (L183, L260, L234A) all are consistent with a kinetic temperature of 10 K and none with temperatures as high as 35 K.

5.2. *Nonthermal Motions*

Figure 6*c* and the values given in Table 8 confirm the well-known observation that molecular lines from interstellar clouds have dispersions in excess of those that can be accounted for by thermal motions, since all the points lie in the region of $\sigma_{\mathrm{NT}} > 0$. However, unlike most of the material in interstellar clouds, these low-mass dense cores are regions where the nonthermal motions are not the dominant motions in the material. Except for TMC-2, the cores are consistent with the thermal motions of the particles of mean mass, which have a dispersion of 0.19 km $\mathrm{s^{-1}}$ at 10 K, exceeding the nonthermal motions.

Fuller & Myers (1992, hereafter FM) showed that the nonthermal part of the velocity dispersion σ_{NT} increases with the map size, for eight cores with associated low-mass stars, and for six cores without such stars, based on observations of lines of NH_3, CS, and $C^{18}O$. This paper discusses an independent probe of kinetic temperature, T_σ, based on observations of NH_3 and HC_3N lines in two cores with associated stars (L483 and L1172) and nine with no associated stars. Only three of the cores discussed here (L1498, L1512, and L234A) are common to the FM sample. Thus the data and results presented here are largely independent of those presented by FM.

Figure 8 shows the variation with map radius of the nonthermal velocity dispersion σ_{NT}, the thermal velocity dispersion σ_T, and the total velocity dispersion σ_{TNT}. Here σ_T and σ_{NT} are based on T_σ, from equation (8) and σ_{TNT} (called σ_{TOT} in FM) is the quadrature sum of σ_T and σ_{NT}. The map radii are those of the NH_3 maps, from BM. In a more accurate treatment, the map radius would reflect both the HC_3N map size and the NH_3 map size. At present only two HC_3N maps are available for comparison with the NH_3 maps (Table 7). The geometric mean of the NH_3 and HC_3N map sizes departs from the NH_3 map size by +15% (L1512) and −13% (L483). These changes would have negligible effect on the scale of Figure 8.

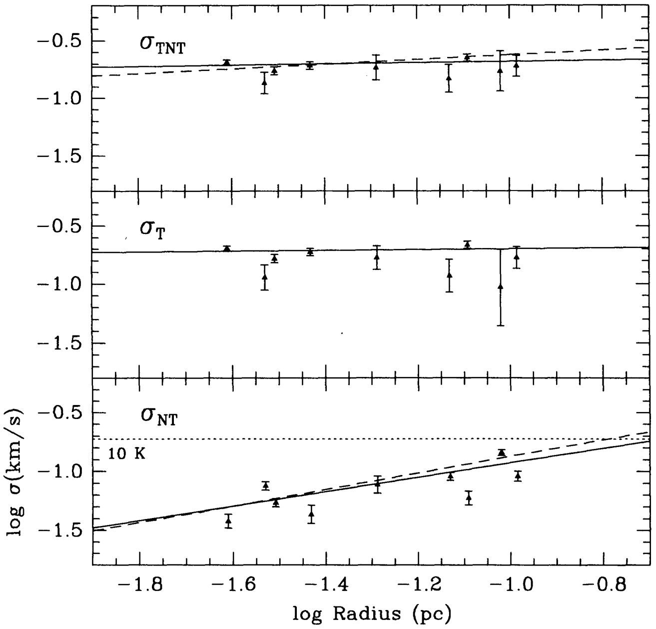

FIG. 8.—The variation of the nonthermal velocity dispersion, σ_{NT}, (*bottom*), the thermal velocity dispersion of the molecule of mean mass, σ_T, (*center*), and the total dispersion of the molecule of mean mass, σ_{TNT}, (*top*) with the radius of the region of ammonia emission. The solid lines show the least-squares fit to the data. The dashed lines show the fits for the variation of the nonthermal and total velocity dispersions found by FM. This figure does not include the observations of L483, L483(a), and TMC-2 and makes use of the optically thin fits for L1517 and L1400K. The dotted horizontal line in the bottom panel indicates the dispersion of the molecule of mean mass at a temperature of 10 K. All the cores have nonthermal motions which are smaller than this value. The error bars show the 1 σ uncertainties.

In Figure 8 the solid lines are the least-squares best linear fits to the log-log plots,

$$\log \sigma_{\mathrm{NT}} = (0.61 \pm 0.06) \log r - (0.31 \pm 0.07)\,, \quad (13)$$

$$\log \sigma_T = (0.03 \pm 0.07) \log r - (0.66 \pm 0.10)\,, \quad (14)$$

$$\log \sigma_{\mathrm{TOT}} = (0.05 \pm 0.07) \log r - (0.63 \pm 0.09)\,. \quad (15)$$

Here the uncertainties are 1 σ values, r is in pc, and each σ is in km $\mathrm{s^{-1}}$. The dashed lines in Figure 8 indicate the corresponding best fits found by FM in their sample. The agreement between the FM fits and the present fits is remarkably good considering that the fits are based primarily on data from different sources and on different methods of temperature measurement.

Following FM we model the number density distribution n as a single power law with radius, and assume spherically symmetric equilibrium to infer the power-law coefficient and exponent from the relation between the velocity dispersion and radius, as in equation (15). We modify the model slightly by assuming hydrostatic equilibrium rather than virial equilibrium, for closer correspondence to the more detailed singular isothermal sphere model of Shu (1977) and to the thermal-nonthermal model of Myers & Fuller (1992, 1993). The resulting density law is equal to that of FM equation (8), multiplied by a factor $2(1-2p)/3$, where p is the velocity-law exponent. For the fit in equation (15), $p = 0.05$ and $n = 35(r/\mathrm{pc})^{-1.9}$. For a typical radius $r = 0.05$ pc, we obtain

$n = 1.0 \times 10^4$ cm^{-3}, less by a factor of 2 than obtained by FM, and still in good agreement with the density needed for excitation of the NH_3 and HC_3N lines. We note that the effect of the nonthermal motions is to make the number density law exponent (-1.9) slightly less steep than expected for a purely isothermal core (-2.0). The steepness of this density law ($\sim r^{-1.9}$) compared to that obtained by FM ($\sim r^{-1.6}$) may be due to the more nearly thermal nature of the gas probed by the lines analyzed here (HC_3N and NH_3) as compared to those analyzed by FM (NH_3, $C^{18}O$, and CS).

There are many potential sources for the nonthermal line broadening, including infall, rotation, outflow, and turbulence. If the nonthermal motions reflect turbulence associated with the magnetic field, these motions can be related to the turbulent magnetic field strength in the foregoing equilibrium model by

$$B = \left[\frac{6(1-4p^2)}{G}\right]^{1/2}\left[\frac{\mathsf{M}}{\mathsf{K}_{\rm NT}}\right]^{1/2} \sigma_{\rm TNT}\, \frac{\sigma_{\rm NT}}{r} \tag{16}$$

where M is the magnetic energy density and $\mathsf{K}_{\rm NT}$ is the nonthermal kinetic energy density. Observations of the Zeeman effect (Myers & Goodman 1988) and other, more indirect, evidence (Bertoldi & McKee 1992) indicate that $\mathsf{M}/\mathsf{K}_{\rm NT}$ is of order unity in many atomic and molecular clouds, and depends on the proportion of magnetic energy in the uniform and nonuniform components of the magnetic field (Myers & Goodman 1991). Assuming that this ratio is 1–2, equation (16) gives

$$\frac{B}{\mu{\rm G}} = 3.5\left(\frac{r}{\rm pc}\right)^{-0.34} = 1.9\left(\frac{n}{{\rm cm}^{-3}}\right)^{0.18}, \tag{17}$$

or $B = 7 - 17$ μG over the range of core sizes 0.02–0.11 pc considered here. These very low field strengths suggest that the thermally dominated cores have much less magnetic energy density than do their environments.

5.3. *The Misfits*

5.3.1. *TMC 2*

TMC-2 is discrepant with the other cores in this study as it is the only core in which the HC_3N dispersion significantly exceeds that of the NH_3. TMC-2 is among the largest NH_3 cores known in the Taurus dark cloud (Myers, Ho, & Benson 1979; Benson & Myers 1989) and may have a more complex structure than some of the other cores in this work. On the Palomar Sky Survey plates TMC-2 appears as one of several regions of high visual extinction in a small filament. TMC-2 is perhaps like one of the other large cores in Taurus, TMC-1, which high-velocity and spatial resolution observations clearly show to be comprised of several distinct clumps (Tölle et al. 1981; Sorochenko et al. 1986; Hirahara et al. 1992). TMC-2 is also distinguished from other cores in that it is associated with a small group of some 10 T Tauri stars (Jones & Herbig 1979) and is one of the strongest sources of HC_5N emission known.

The residuals from the HC_3N fit show no evidence for any additional velocity components. If the enhanced line width of the HC_3N is due to the HC_3N tracing a larger region of the core, then it is estimated that the HC_3N emission region should be about 3 times the size of the NH_3 emission region, based on the correlation of nonthermal velocity dispersion with size determined for dense cores by FM. Clearly testing of this hypothesis awaits a complete map of the HC_3N emission toward this core.

TABLE 9

L483 Two-Component NH_3 Fit

A (K) (1)	τ (nepers) (2)	$V_{\rm LSR}$ (km s^{-1}) (3)	σ (km s^{-1}) (4)
0.50(0.06).........	30(5)	5.301(0.007)	0.105(0.006)
0.67(0.06).........	12(1)	5.58(0.02)	0.180(0.009)

Cols. (1)–(4) are defined in the text (§ 3). The values in parentheses are the 1 σ uncertainties.

5.3.2. *L483*

L483 is the only core in this study for which there are two pairs of high-resolution measurements and hence temperature determinations at two positions within a core. Unlike TMC-2, both positions in L483 are consistent with a model of the two species tracing the same material with the two species having the same nonthermal motions. However, at both positions the temperature determined from the line widths is considerably in excess of the excitation temperatures. At the position called L483, which corresponds to the peak of the NH_3 emission and the location of the young star in the core, $T_\sigma = 63 \pm 6$ K. One arcminute west of this position at L483(a), $T_\sigma = 25 \pm 3$ K. At both these positions the HC_3N and NH_3 excitation temperatures are between 6 and 9 K.

The high line width temperatures at these two positions suggest that the NH_3 line is broader than expected compared to the HC_3N line and a temperature of 10 K. Examining the fit to the NH_3 line at the peak of the core (Table 6) shows that the fit has the largest χ^2 of any observation. The residuals of this single-component fit show considerable structure. A two-component fit at this position reduces the χ^2 to 575 when using 501 data points in the fit. The parameters of the two-component fit are given in Table 9. There is no indication of a second velocity component in the HC_3N spectrum at this position.

The narrower and weaker component of the two NH_3 velocity components is at a velocity only 0.06 km s^{-1} larger than the HC_3N velocity, whereas the stronger, broader component is shifted by 0.34 km s^{-1} compared to the HC_3N. It therefore appears that the narrow, weak component is associated with the gas traced by the HC_3N. Using the dispersion of this component and the HC_3N velocity dispersion in equation (8) gives $T_\sigma = -18 \pm 5$ which, as for TMC-2, indicates that assumptions of the model are incorrect in the sense that the HC_3N dispersion is too large compared to the NH_3 dispersion. The HC_3N could have a larger velocity dispersion than the NH_3, and be consistent with the two-component model, if the 5.30 km s^{-1} NH_3 emission traces a smaller, unresolved region with smaller nonthermal motions within the core. This, however, seems unlikely since 1′ west at L483(a) the NH_3 line velocity is 5.38 km s^{-1}, suggesting that the material at this velocity is extended and that it is the 5.58 km s^{-1} component which is compact. Alternatively, the HC_3N could have an enhanced line width due to the action of the outflow from the young star on the core material at the smaller size scale than traced by the NH_3.

6. CONCLUSIONS

Observations of the HC_3N $J = 4 \rightarrow 3$ transition show it to be useful probe of the densest regions of dense cores. The presence of resolvable hyperfine structure allows the optical depth of the transition to be determined, which is important in understanding the excitation of the transition and the role of any optical depth effects in determining the shape of the line profile. This transition is similar in several respects to the better studied NH_3 (1, 1) transition which traces similar regions of dense cores. The HC_3N transition has line widths similar to, but smaller than, those of the NH_3 (1, 1) transition. There is substantial overlap of the regions of emission from these two tracers in two cores which have been mapped in both transitions. In addition, the velocities of the two transitions typically differ by less than a line width. These observations indicate that HC_3N $J = 4 \rightarrow 3$ traces the same thermal material in dense cores as NH_3 (1, 1). However, the small physical extent of the dense, thermal regions in dense cores means that the increased angular resolution obtainable due to the higher frequency of the HC_3N transition is a significant advantage over the NH_3 transition for studying these regions.

The observations show the HC_3N and NH_3 fit a simple model in which both transitions are tracing material of a single kinetic temperature with the same nonthermal motions. Assuming that the nonthermal motions are the same for both transitions, both the dispersion of the nonthermal motions and the kinetic temperature have been determined at 12 positions in 11 dense cores. For nine of these positions the derived kinetic temperature is consistent with the excitation temperatures estimated from the line brightness for both the HC_3N and NH_3 transitions. These nine cores have a weighted mean kinetic temperature of 9.2 K with a standard deviation of 0.6 K. The nonthermal velocity dispersions range from 0.043 ± 0.007 km s^{-1} to 0.145 ± 0.008 km s^{-1}.

The similarity of the line width–determined kinetic temperatures and the line excitation temperatures implies that the number density of the regions traced by the HC_3N is about 3×10^4 cm^{-3}, consistent with the density determined from NH_3 observations and considerably lower than the determinations from CS observations by Zhou et al. (1989) of similar cores.

Analysis of the variation of the velocity dispersion with the size of the emission region indicates that the nonthermal velocity dispersion increases as the 0.6 ± 0.1 power of the map size, while the total velocity dispersion increases as the 0.05 ± 0.07 power of the map size. Although these variations with map size are based on a different and larger sample of cores, the relations are consistent with those found by FM. In an equilibrium model, these relations correspond to a number density profile, $n \sim r^{-1.9}$, which is very close to an isothermal density profile. The magnetic field whose energy density equals that of the nonthermal motions has a typical strength of 10 μG over the range of cores sizes 0.02–0.11 pc.

G. A. F. acknowledges the support of a Center for Astrophysics Postdoctoral Fellowship and a National Radio Astronomy Observatory Jansky Fellowship. We would like to thank the many people at the Haystack Observatory who made the observations reported here possible. In addition, we wish to thank A. Wootten for carefully reading this manuscript, P. Benson for supplying the NH_3 map of L483, and M. Gordon for helpful discussions.

REFERENCES

Adams, F. C., Lada, C. J., & Shu, F. H. 1987, ApJ, 312, 788
Baade, W., Goos, F., Koch, P. P., & Minsowski, R. 1933, Z. Astroph, 6, 355
Barrett, A. H., Meeks, M. L., & Weinreb, S. 1964, Nature, 202, 475
Beichman, C. A., Myers, P. C., Emerson, J. P., Harris, S., Mathieu, R. D., Benson, P. J., & Jennings, R. E. 1986, ApJ, 307, 337
Benson, P. J. 1983, Ph.D. thesis, Massachusetts Institute of Technology
Benson, P. J., & Myers, P. C. 1983, ApJ, 270, 589
———. 1989, ApJS, 71, 89 (BM)
Bertoldi, F., & Mckee, C. F. 1992, ApJ, 395, 140
Butner, H., Lada, E. A., & Loren, R. B. 1993, ApJ, submitted
Cox, P., Walmsley, C. M., & Güsten, R. 1989, A&A, 209, 382
Cresswell, R. A., Winnewisser, G., & Gerry, M. C. L. 1977, J. Molec. Spectrosc., 65, 420
Fiebig, D. 1990, Ph.D. thesis, Rheinischen Friedrich-Wilhelms-Universität, Bonn
Frerking, M. A., Langer, W. D., & Wilson, R. W. 1987, ApJ, 313, 320
Fuller, G. A. 1989, Ph.D. thesis, Univ. California, Berkeley
Fuller, G. A., & Myers, P. C. 1992, ApJ, 384, 523 (FM)
Goodman, A. A., Benson, P. J., Fuller, G. A., & Myers, P. C. 1993, ApJ, 406, 528
Gordon, M. A. 1976, Methods Exper. Phys., 12C, 277
Gordon, M. A., & Churchwell, E. 1970, A&A, 9, 307
Green, S., & Chapman, S. 1978, ApJS, 37, 169
Hirahara, Y., et al. 1992, ApJ, 394, 539
Ho, P. T. P. 1977, Ph.D. thesis, Massachusetts Institute of Technology
Ho, P. T. P., & Townes, C. H. 1983, ARA&A, 21, 239
Jones, B. F., & Herbig, G. H. 1979, AJ, 84, 1872
Kukolich, S. G. 1967, Phys. Rev., 156, 83
Lafferty, W. J., & Lovas, F. J. 1978, J. Phys. Chem. Ref. Data, 7, 441
Little, L. T., Macdonald, G. H., Riley, P. W., & Matheson, D. N. 1979, MNRAS, 189, 539
Myers, P. C. 1983, ApJ, 270, 105
Myers, P. C., & Benson, P. J. 1983, ApJ, 266, 309
Myers, P. C., & Fuller, G. A. 1992, ApJ, 396, 631
———. 1993, ApJ, 402, 635
Myers, P. C., & Goodman, A. A. 1988, ApJ, 329, 392
———. 1991, ApJ, 373, 509
Myers, P. C., Fuller, G. A., Goodman, A. A., & Benson, P. J. 1991, ApJ, 376, 561
Myers, P. C., Fuller, G. A., Mathieu, R. D., Beichman, C. A., Benson, P. J., Schild, R. E., & Emerson, J. P. 1987, ApJ, 319, 349
Myers, P. C., Ho, P. T. P., & Benson, P. J. 1979, ApJ, 233, 141
Parker, N. D. 1988, MNRAS, 235, 139
Pauls, T. A., Wilson, T. L., Bieging, J. H., & Martin, R. N. 1983, A&A, 124, 23
Shu, F. H. 1977, ApJ, 214, 488
Sorochenko, R. L., Tolmachev, A. M., & Winnerwisser, G. 1986, A&A, 155, 237
Suzuki, H., Yamamoto, S., Ohishi, M., Kaifu, N., Ishikawa, S., Hirahara, Y., & Takano, S. 1992, ApJ, 392, 551
Thum, C. 1980, in Radio Recombination Lines, ed. P. A. Shaver (Dordrecht: Reidel), 50
Tölle, F., Ungerechts, H., Walmsley, C. M., Winnewisser, G., & Churchwell, E. 1981, A&A, 95, 143
Ungerechts, H., Walmsley, C. M., & Winnewisser, G. 1990, A&A, 88, 259
Zhou, S., Wu, Y., Evans, N. J., Fuller, G. A., & Myers, P. C. 1989, ApJ, 346, 168